

Letters

Depth-Adaptive Object Identification Using Terahertz Time-Domain Spectroscopic Data

Kanto Kito, Takamaru Matsui, and Shouhei Kidera 

Abstract—This study focused on machine-learning-based object recognition using the terahertz (THz) band time-domain spectroscopy (TDS) measurements. The reflection responses from each object showed severe depth dependence due to the out-of-focus effect, which was hardly compensated in the analytical propagation model. Such depth dependence severely limits the application range of THz-TDS-based object recognition, where the depth adjustment is not easily achieved, such as in subsurface imaging or industrial product inspection in an assembly line. In this study, we developed a simple adaptive depth signal conversion scheme using a calibration object before neural-network-based supervised learning. Experimental validations using several mono- or disaccharides and their THz-TDS data demonstrated that our compensation scheme successfully enhanced the recognition ratio.

Index Terms—Depth-adaptive conversion, object recognition, spectroscopic imaging, submillimeter wave, terahertz (THz) wave.

I. INTRODUCTION

Terahertz (THz) band waves, which are electromagnetic waves from 100 GHz to 10 THz, are located in the frequency domain between near-infrared light and millimeter waves; thus, THz band waves provide both microscale spatial resolution and millimeter-class penetration depth. Thus, this imaging technology is promising for various applications such as the noninvasive medical diagnosis of skin diseases [1]–[3], the determination of prohibited drugs [4], or the pesticide detection [5], based on chemical composition analysis using spectroscopic information. By focusing on chemical compound analysis or polymer identification, supervised machine learning approaches such as neural networks (NNs) have been developed by exploiting the spectroscopic feature originating from a chemical compound. Several studies have focused on target identification or recognition using THz time-domain spectroscopy (THz-TDS) data such as hepatic tumor detection [6], chemical

compound analysis [7]–[9], transgenic ingredients [10], and other materials [11], [12].

However, the aforementioned approaches assume that the reflection responses are observed in situations, in which the focal depth point is accurately adjusted within a 1-mm scale. Most THz imaging systems (e.g., THz-TDS) require prior mechanical adjustment to ensure that the focal point is on the target surface; this process narrows the possible applications, where the surface depth would vary according to the measurement sequences, such as industrial product inspection on the assembly line or embedded object recognition. However, to the best of our knowledge, there is no literature focusing on object identification. Additionally, several studies [13] have demonstrated that a reflection signal has significant dependence on the depth of the reflection point; this is caused by electromagnetic interference effects such as caustic effects or the aberration of the dielectric lens. Thus, these depth-dependent effects incur a lower recognition performance when the training data are selected from a dataset containing only on-focus reflections. One can conceive that these dependencies can be compensated for by an analytical approach using Green's function; however, the aforementioned propagation effect is hardly a model of analytical form because it depends on the actual dielectric design of the transmitter and receiver lens. To overcome this problem, this study introduces a simple depth conversion scheme using the transfer function, which was preliminarily attained from a reflection of the reference target, such as a metallic plate. Notably, while our previous study [13] focused on issues with multilayer structure analysis, where the material thickness was analyzed by measuring the unfocused depth, this study handled a different problem of object identification at the unfocused depth issue using a machine learning scheme. Our THz-TDS experiments on four different types of polymers enclosed in a small capsule confirmed that our depth compensation approach remarkably enhances the recognition grade compared with that obtained without depth compensation, namely, the conventional approach.

II. METHOD

A. Adaptive Depth Conversion Scheme

In this study, we assume a THz-TDS measurement model, in which the focal depth is defined as D_{foc} . Assuming a number

Manuscript received February 14, 2021; revised April 6, 2021; accepted April 29, 2021. Date of publication May 11, 2021; date of current version September 2, 2021. This work was supported by Japan Science and Technology Agency's Precursory Research for Embryonic Science and Technology under Grant JPMJPR1771. (Corresponding author: Shouhei Kidera.)

The authors are with the Graduate School of Informatics and Engineering, University of Electro-Communications, Tokyo 1828585, Japan (e-mail: kito.kanto@ems.cei.uec.ac.jp; matsui.takamaru@ems.cei.uec.ac.jp; kidera@uec.ac.jp).

Color versions of one or more figures in this article are available at <https://doi.org/10.1109/TTHZ.2021.3078880>.

Digital Object Identifier 10.1109/TTHZ.2021.3078880

of unknown polymer targets, our method identifies the chemical material using the backscattered reflection signal. Considering the reflection signal from a target located at a depth of D , $s(t; D)$ denotes the recorded electric field measured at the receiver lens.

There are various approaches for object recognition using frequency responses provided by THz-TDS; however, a target's frequency characteristic largely depends on the depth of the object. In particular, the frequency response at an out-of-focus depth is significantly different from that obtained at an on-focus depth. This depth dependence characteristic would be hardly modeled by an analytical form, because such an effect is caused by the electromagnetic interference, caustic effect, or the aberration effects due to wideband THz beam and would be affected by the actual design of a transmitter and receiver lens, including the supporting device. According to this background, this study first introduces a simplified depth-adaptive conversion scheme from off- to on-focus observation, using the reference signal based calibration with a linear transfer function model. In this method, we use the reflection responses from reference target, such as a metallic plate or an empty capsule, at different depths. Let $S_{\text{ref}}(\omega; D_{\text{foc}})$ and $S_{\text{ref}}(\omega; D)$ be as the complex-valued reflection responses from the reference target at depths for the on-focus D_{foc} and off-focus D , respectively. The frequency dependence due to different depth reflection is compensated via the following transfer function:

$$\hat{S}(\omega; D_{\text{foc}}) = \frac{S_{\text{ref}}(\omega; D_{\text{foc}})}{S_{\text{ref}}(\omega; D)} \times S(\omega; D) \quad (1)$$

where $S(\omega; D)$ denotes the reflection response from the unknown target at depth D .

B. NN-Based Identification

Focusing on object recognition using the above frequency responses, this study introduces an NN-based classifier as follows. The NNs are well known as promising supervised and nonlinear classifiers introduced in many studies for the THz band [14]–[16]. The most distinguished advantage of the NN is that high-dimensional input data could be classified via the nonlinear activation function based on the number of hidden layers with numerous neurons. The proposed NN scheme is described as follows.

Here, the input vector \mathbf{X} for the machine learning identification is defined as follows:

$$\mathbf{X} \equiv [\text{Re}[\hat{S}(\omega_1; D_{\text{foc}})], \dots, \text{Re}[\hat{S}(\omega_N; D_{\text{foc}})], \text{Im}[\hat{S}(\omega_1; D_{\text{foc}})], \dots, \text{Im}[\hat{S}(\omega_N; D_{\text{foc}})]]^T \quad (2)$$

where N denotes the total number of frequency points, thus covering the effective bandwidth of the received signal. Note that the input vector is only used for the reflection signal at the depth D_{foc} ; specifically, training data at the difference depth reflection are not necessary for this method, which is one of the most significant advantages of our proposed method.

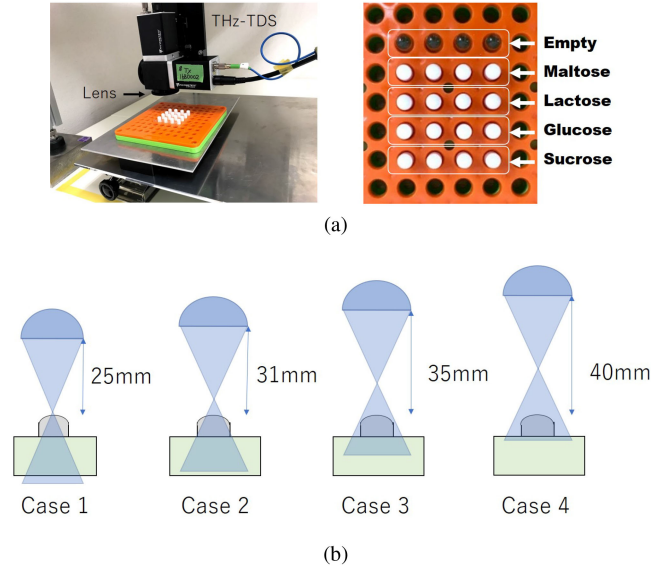


Fig. 1. (a) and (b) Right: Measurement setup with the THz-TDS system. Left: Arrangement of objects enclosed plastic capsule.

III. RESULTS AND DISCUSSIONS

A. Experimental Setup

Fig. 1 shows the measurement setup and object arrangement using the THz-TDS system provided by Spectra Design Co., Ltd. Four types of objects, namely, lactose, maltose, glucose, and sucrose, were used. To collect the number of data samples, each object was enclosed in a plastic capsule and was located at four different locations, as shown in Fig. 1, including the empty capsule. A photoconductive dielectric lens antenna, which had a 25-mm focal depth, was scanned on the plane with a fixed interval of 0.25 mm. The transmitted pulse-modulated signal had a frequency range of 0.05–0.2 THz, i.e., 0.15-THz 3-dB bandwidth. As the training or test data input, the complex frequency responses from 0.1–0.2 THz are sampled with a 6.25-GHz interval, namely, 17 frequency samples were extracted. In particular, the training dataset is extracted from only $S_{\text{ref}}(\omega; D_{\text{foc}})$ and $S(\omega; D_{\text{foc}})$, namely, the reflection responses from the reference and four different objects at focal depth $D = 25$ mm.

Four different depths of 25 mm (Case 1), 31 mm (Case 2), 35 mm (Case 3), and 40 mm (Case 4) were investigated, where Case 1 corresponds to the on-focus case. For adaptive depth conversion, we prepared two types of reference targets at each depth. One was the reflection signal from the metallic plate with a 99.5-mm width, 14.95-mm length, and 1.57-mm thickness, called “Reference A,” and the other was that from the empty capsule called “Reference B.” Fig. 2 shows the frequency responses for the objects and reference target at different depths. As shown in this figure, there was significant dependence on the observation depth, particularly in the case of the off-focus, and the 3-dB bandwidths became considerably narrower than that of the on-focus signal. It was considered that an aberration effect causes incoherency among different wavelengths at the out-of-focus depth. Thus, if the input vectors are not compensated for at the off-focus signal, the recognition rate

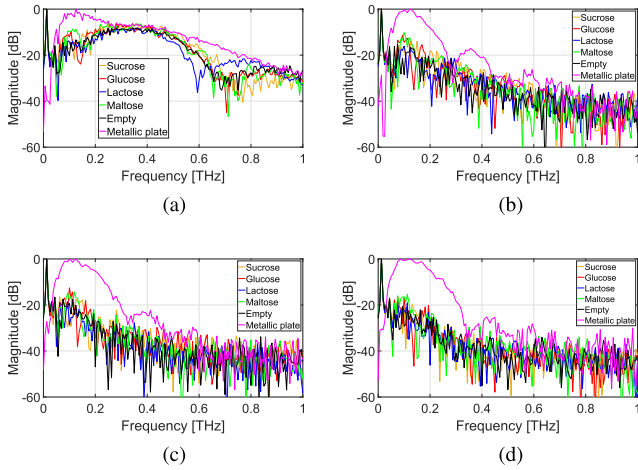


Fig. 2. Frequency responses at different depths from each object. (a) $D = 25$ mm. (b) $D = 31$ mm. (c) $D = 35$ mm. (d) $D = 40$ mm.

would be downgraded because of the above mismatch of the frequency response. Note that it is extremely difficult to simulate the frequency spectrum at each depth for referential data in Fig. 2, because it is impractical to simulate the spatial area over 200 mm (200 wavelengths), including the photo-conductive antenna (PCA) and objects, using a reliable forward solver, such as the 3-D finite-difference time-domain analysis. However, there are many open databases to investigate the frequency responses as to absorbance or transmittance, such as <http://thzdb.org/> or <https://webbook.nist.gov/chemistry/thz-ir/>, including these frequency bands.

B. Results

1) *Depth Conversion*: First, we investigated the depth conversion results using (1) as follows. Figs. 3–6 show the results of the adaptive depth conversions for all materials at different depths, and these demonstrated that our compensation scheme successfully reconstructed the on-focus reflection from the off-focus signal at any depth according to (1). From these figures, we could confirm that the converted data using Reference A provide a more accurate reconstruction of the focal depth at 25 mm, especially for $D = 35$ and $D = 40$ mm, compared with those obtained using Reference B. In addition, focusing on the higher frequency range at 0.2 THz, Reference B could not offer an accurate reconstruction because it is the reflection from the empty capsule, and its bandwidth is narrower than that of Reference A (see Fig. 2); therefore, it suffers from low signal-to-noise ratio (SNR) in a high-frequency range. To validate our method, the following quantitative criteria with the normalized root-mean-square errors (NRMSE) for the response reconstruction are introduced as follows:

$$\text{NRMSE} = \sqrt{\frac{\sum_{i=1}^N |S(\omega_i; D_{\text{foc}}) - \hat{S}(\omega_i; D_{\text{foc}})|^2}{\sum_{i=1}^N |S(\omega_i; D_{\text{foc}})|^2}} \quad (3)$$

where N denotes the number of frequency samples, which was 17 in this case. Tables I–III show the NRMSE for each depth and reference target. In this study, a reflection response from each target $S(\omega, D)$, e.g., sucrose, is converted to the focused

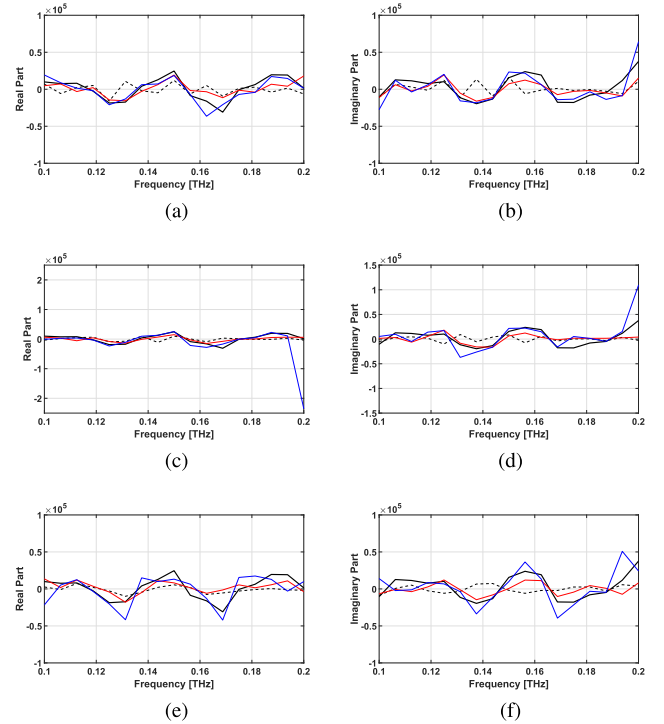


Fig. 3. Real and imaginary parts of complex-valued frequency responses at the case of “sucrose,” with or without adaptive depth conversion at the different depths. Black, red, and blue lines denote $S(\omega; D_{\text{foc}})$, $\hat{S}(\omega; D_{\text{foc}})$ with “Reference A,” and $\hat{S}(\omega; D_{\text{foc}})$ with “Reference B,” respectively. Black dot line denotes $S(\omega; D)$. (a) $D = 31$ mm. (b) $D = 31$ mm. (c) $D = 35$ mm. (d) $D = 35$ mm. (e) $D = 40$ mm. (f) $D = 40$ mm.

TABLE I
NRMSE AT THE DEPTH OF $D = 31$ mm

Object	Sucrose	Glucose	Lactose	Maltose
Raw data	0.9605	1.0863	1.0625	1.0234
Reference A	0.6647	0.6103	0.7752	0.5066
Reference B	0.6001	1.2614	1.0642	0.8738

TABLE II
NRMSE AT THE DEPTH OF $D = 35$ mm

Object	Sucrose	Glucose	Lactose	Maltose
Raw data	0.9979	1.105	1.0081	1.0302
Reference A	0.7412	0.7021	0.8194	0.6103
Reference B	2.7455	3.2674	2.1488	2.4990

TABLE III
NRMSE AT THE DEPTH OF $D = 40$ mm

Object	Sucrose	Glucose	Lactose	Maltose
Raw data	0.9741	1.0591	1.0047	0.9741
Reference A	0.7531	0.7565	0.8041	0.6579
Reference B	0.9044	1.5861	1.4858	1.1492

data as $S(\omega, D_{\text{foc}})$ in (1), using both reference signals of the focused and unfocused depths, denoted as $S_{\text{ref}}(\omega; D_{\text{foc}})$ and $S_{\text{ref}}(\omega; D)$, respectively, where References A and B are tested. These tables demonstrate that the proposed conversion scheme using Reference A could reconstruct the depth dependence component, compared with that using Reference B, which would contribute to upgrading the recognition performance.

2) *Object Identification*: Next, the object identifications are tested as follows. Fig. 7 shows the details of the NN structure

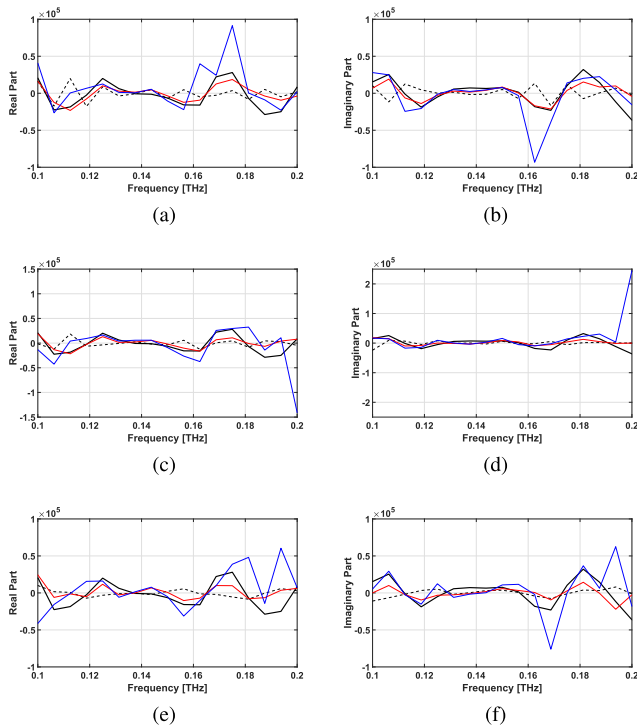


Fig. 4. Real and imaginary parts of complex-valued frequency responses at the case of “glucose,” with or without adaptive depth conversion at the different depths. Black, red, and blue lines denote $S(\omega; D_{foc})$, $\hat{S}(\omega; D_{foc})$ with “Reference A,” and $\hat{S}(\omega; D_{foc})$ with “Reference B,” respectively. Black dot line denotes $S(\omega; D)$. (a) $D = 31$ mm. (b) $D = 31$ mm. (c) $D = 35$ mm. (d) $D = 35$ mm. (e) $D = 40$ mm. (f) $D = 40$ mm.

TABLE IV
CONFUSION MATRIX USING REFERENCE A ($D = 31$ mm)

		Predicted			
		Sucrose	Glucose	Lactose	Maltose
Actual	Sucrose	71.2 %	0 %	0 %	0 %
	Glucose	0 %	100 %	0 %	0 %
	Lactose	28.8 %	0 %	100 %	1.8 %
	Maltose	0 %	0 %	0 %	98.2 %

assumed in this test. We assume one input, hidden, and output layers for simplicity, where the number of neurons of the hidden and output layers is ten and four, respectively. The backpropagation approach is employed in the training phase, where the scaled conjugate gradient optimization is implemented [17]. Regarding input data sampling, since the set of PCA transmitter and receiver is scanned on the plane at the depth of 0 mm, we determine the ten sampling points that offer the largest magnitude of the THz-TDS response $s(t; D_{foc})$ at 25-mm depth for each target, which are the training dataset in the proposed NN. Fig. 8 shows the sampling data extraction scheme from the focused THz-TDS image for each object. The test samples are extracted from the unfocused case as 1 mm (Case 2), 35 mm (Case 3), and 40 mm (Case 4) with the same process. Then, the total training and test samples are extracted as ten samples from four objects; hence, the total numbers of them are both 40.

Tables IV–XII show the examples of the 4×4 confusion matrices in each depth and with each reference signal. In addition, we investigated 100 training trials because the optimization

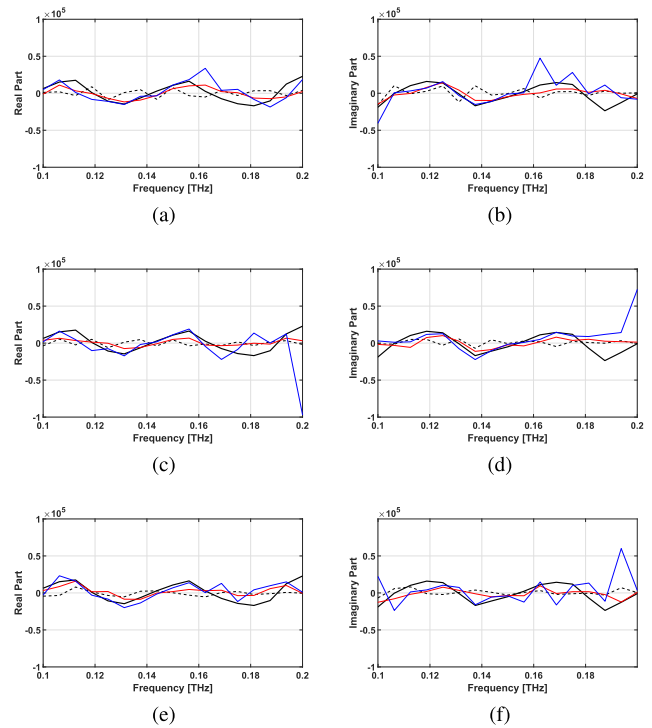


Fig. 5. Real and imaginary parts of complex-valued frequency responses at the case of “lactose,” with or without adaptive depth conversion at the different depths. Black, red, and blue lines denote $S(\omega; D_{foc})$, $\hat{S}(\omega; D_{foc})$ with “Reference A,” and $\hat{S}(\omega; D_{foc})$ with “Reference B,” respectively. Black dot line denotes $S(\omega; D)$. (a) $D = 31$ mm. (b) $D = 31$ mm. (c) $D = 35$ mm. (d) $D = 35$ mm. (e) $D = 40$ mm. (f) $D = 40$ mm.

process in the training step includes a random search process at the initial step; thus, each training result is variable to a random number seed. Fig. 9 shows the box plots for the recognition rates of target identification using 100 confusion matrices. Here, the vertical axis of these box plots, namely, the recognition rate, denotes the average of the sensitivities for four materials, that is, the averages of the diagonal components of 100 confusion matrices as from Tables IV–XII. Note that the box plot test has been massively introduced in many studies in the machine learning field [18]–[20], which has been admitted as one of the most reliable statistical criteria in handling the asymmetric probabilistic distribution having some outliers. The median values of the recognition rates for the depth of 31, 35, and 40 mm are 97.5%, 100%, and 90% for Reference A, 100%, 40%, and 58.75% for Reference B, and 25%, 25%, and 25% for the raw data, respectively. These box plots and median values demonstrate that our proposed method, especially using Reference A, remarkably upgraded the recognition rates in all cases, above 90%. For Reference B, the results suffered from lower recognition rate for the cases of 35 and 40 mm because reflection from the empty capsule included some multiple scattering effects inside the capsule, which might not have been included in reflections from the polymer capsule. On the contrary, in the case of 31 mm, the conversion scheme using Reference B attains the highest recognition rate as in Fig. 9(a), which is because the reflection signals in the case of 31 mm have relatively large SNR, compared with those obtained at 35 or 40 mm, and its

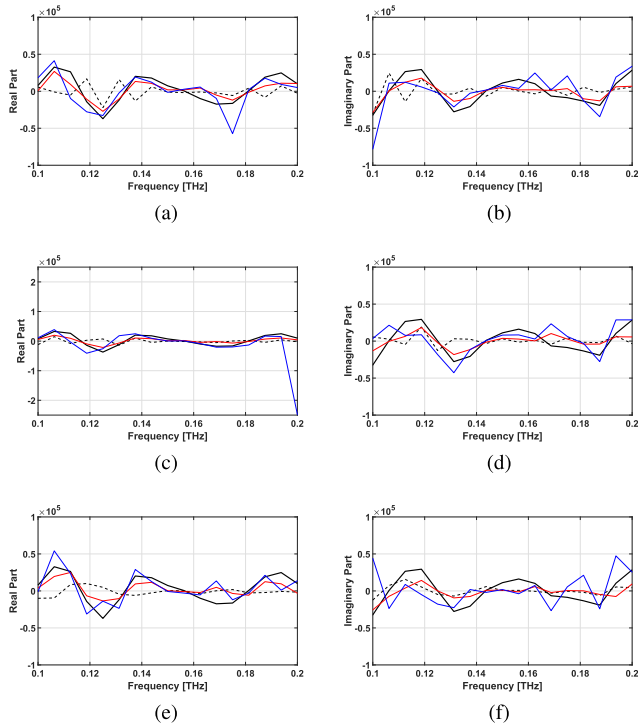


Fig. 6. Real and imaginary parts of complex-valued frequency responses at the case of “maltose,” with or without adaptive depth conversion at the different depths. Black, red, and blue lines denote $S(\omega; D_{foc})$, $\hat{S}(\omega; D_{foc})$ with “Reference A,” and $\hat{S}(\omega; D_{foc})$ with “Reference B,” respectively. Black dot line denotes $S(\omega; D)$. (a) $D = 31$ mm. (b) $D = 31$ mm. (c) $D = 35$ mm. (d) $D = 35$ mm. (e) $D = 40$ mm. (f) $D = 40$ mm.

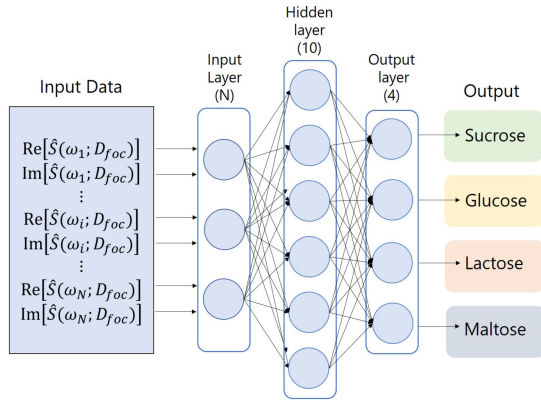


Fig. 7. Structure of a neural network.

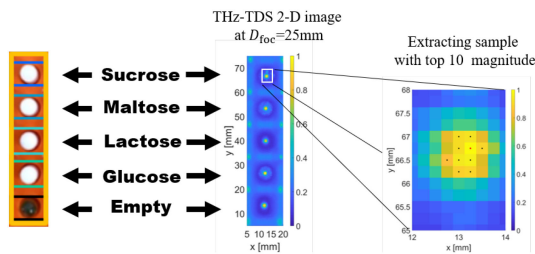


Fig. 8. Data sampling scheme from the focused THz-TDS image.

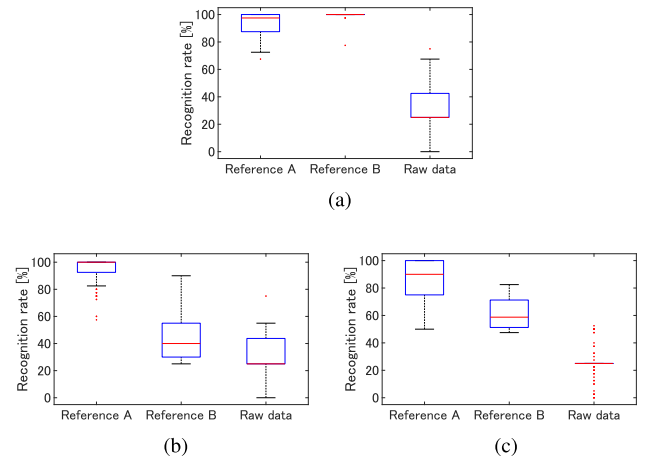


Fig. 9. Box plots of recognition accuracies at different depths. Red line: Median. Lower and upper boundaries of box denote 25% and 75%. Lower and upper whiskers denote the ± 2.7 standard deviation range, respectively. Red cross points are outlier over the whiskers. (a) $D = 31$ mm. (b) $D = 35$ mm. (c) $D = 40$ mm.

TABLE V
CONFUSION MATRIX USING REFERENCE A ($D = 35$ mm)

Actual \ Predicted	Sucrose	Glucose	Lactose	Maltose
Sucrose	85.6 %	0 %	1.8 %	0 %
Glucose	0.8 %	100 %	1.7 %	0 %
Lactose	13.6 %	0 %	96.5 %	6.7 %
Maltose	0 %	0 %	0 %	93.3 %

TABLE VI
CONFUSION MATRIX USING REFERENCE A ($D = 40$ mm)

Actual \ Predicted	Sucrose	Glucose	Lactose	Maltose
Sucrose	75.9 %	0 %	0 %	0.7 %
Glucose	0.4 %	100 %	1.4 %	0 %
Lactose	23.7 %	0 %	98.6 %	30.7 %
Maltose	0 %	0 %	0 %	68.6 %

TABLE VII
CONFUSION MATRIX USING REFERENCE B ($D = 31$ mm)

Actual \ Predicted	Sucrose	Glucose	Lactose	Maltose
Sucrose	100 %	0.1 %	0 %	0 %
Glucose	0 %	99 %	0 %	0 %
Lactose	0 %	0.9 %	100 %	0.1 %
Maltose	0 %	0 %	0 %	99.9 %

frequency responses are not too far from those obtained from focused 25-mm depth, even when using Reference B, where a multiple scattering between the upper and lower sides of capsule might be negligible. Nonetheless, we clearly demonstrated that the depth conversion scheme is considerably effective compared with those not using this scheme.

Furthermore, we investigated the case using different frequency ranges of the input data in the proposed NN process. Considering the frequency responses of each depth, we extract the frequency range of 0.05–0.25 THz, which still has significant responses compared with other bands (see Fig. 2). Fig. 10 shows the box plot in this case, where each indication is defined as in

TABLE VIII
CONFUSION MATRIX USING REFERENCE B ($D = 35$ mm)

Actual \ Predicted	Sucrose	Glucose	Lactose	Maltose
Sucrose	95.8 %	83.7 %	83.9 %	37.8 %
Glucose	1.2 %	15.8 %	0.7 %	9.9 %
Lactose	0 %	0 %	11.3 %	0 %
Maltose	3 %	0.5 %	4.1 %	52.3 %

TABLE IX
CONFUSION MATRIX USING REFERENCE B ($D = 40$ mm)

Actual \ Predicted	Sucrose	Glucose	Lactose	Maltose
Sucrose	99 %	95 %	49.8 %	1 %
Glucose	0 %	4.6 %	1.2 %	0 %
Lactose	0 %	0 %	44.1 %	0 %
Maltose	1 %	0.4 %	4.9 %	99 %

TABLE X
CONFUSION MATRIX USING RAW DATA ($D = 31$ mm)

Actual \ Predicted	Sucrose	Glucose	Lactose	Maltose
Sucrose	14.9 %	0 %	8.9 %	15.7 %
Glucose	34.1 %	44.3 %	35.1 %	59.1 %
Lactose	50.5 %	26 %	56 %	25.2 %
Maltose	0.5 %	29.7 %	0 %	0 %

TABLE XI
CONFUSION MATRIX USING RAW DATA ($D = 35$ mm)

Actual \ Predicted	Sucrose	Glucose	Lactose	Maltose
Sucrose	8.2 %	3.1 %	3.9 %	12 %
Glucose	41 %	38.7 %	23.4 %	30.1 %
Lactose	48.5 %	49.3 %	69.9 %	50.9 %
Maltose	2.3 %	8.9 %	2.8 %	7 %

TABLE XII
CONFUSION MATRIX USING RAW DATA ($D = 40$ mm)

Actual \ Predicted	Sucrose	Glucose	Lactose	Maltose
Sucrose	2.9 %	0.8 %	6.8 %	10.3 %
Glucose	52 %	43.6 %	38 %	33 %
Lactose	38.9 %	48.4 %	50.5 %	54 %
Maltose	6.2 %	7.2 %	4.7 %	2.7 %

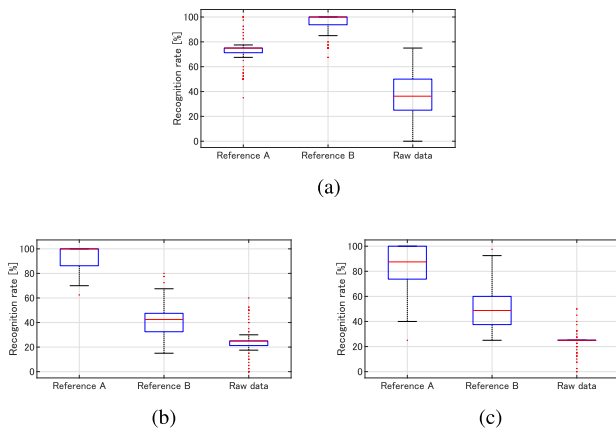


Fig. 10. Box plots of recognition accuracies at different depths at the frequency range from 0.05 to 0.25 THz. Red line: Median. Lower and upper boundaries of box denote 25% and 75%. Lower and upper whiskers denote the ± 2.7 standard deviation range, respectively. Red cross points are outlier over the whiskers. (a) $D = 31$ mm. (b) $D = 35$ mm. (c) $D = 40$ mm.

Fig. 9. Fig. 9 also demonstrated that our depth-adaptive conversion scheme would be effective in wideband inputs; especially, the conversion with Reference A would offer a high recognition rate in any depth. Notably, while we can choose the data with a high frequency above 0.5 or 1.0 THz, the responses would be highly contaminated by the noise, and we consider that they could not provide meaningful results or discussions in this case because the training performance of the proposed NN would experience overfitting phenomena.

IV. CONCLUSION

This study focused on the THz-TDS data-based identification of objects using a supervised NN approach, assuming that the depth of the target could not be accurately adjusted to the focal depth, such as during product inspection in an assembly line or the recognition of a buried object embedded in plastic or paper. To achieve depth-free recognition, this study newly introduces transfer-function-based depth-adaptive conversion using the reflection signals from reference targets at different depths. For the experimental tests, with identification of four types of objects, our method accurately converted the off-focus reflection to on-focus signals, which were input into NN-based learning. The notable feature of this method is that we only need to measure the reflection signals from metallic plates at possible depths, thus avoiding the additional acquisition of training data at each depth.

REFERENCES

- [1] K. I. Zaytsev, A. A. Gavdush, N. V. Chernomyrdin, and S. O. Yurchenko, "Highly accurate in vivo terahertz spectroscopy of healthy skin: Variation of refractive index and absorption coefficient along the human body," *IEEE Trans. THz Sci. Technol.*, vol. 5, no. 5, pp. 817–827, Sep. 2015.
- [2] B. C. Q. Truong, H. D. Tuan, V. P. Wallace, A. J. Fitzgerald, and H. T. Nguyen, "The potential of the double debye parameters to discriminate between basal cell carcinoma and normal skin," *IEEE Trans. THz Sci. Technol.*, vol. 5, no. 6, pp. 990–998, Nov. 2015.
- [3] K. Yang, N. Chopra, Q. H. Abbasi, K. A. Qaraqe, and A. Alomainy, "Collagen analysis at terahertz band using double-debye parameter extraction and particle swarm optimisation," *IEEE Access*, vol. 5, pp. 27850–27856, 2017.
- [4] K. W. Kim, H. Kim, J. Park, J. K. Han, and J. Son, "Terahertz tomographic imaging of transdermal drug delivery," *IEEE Trans. THz Sci. Technol.*, vol. 2, no. 1, pp. 99–106, Jan. 2012.
- [5] Y. Hua and H. Zhang, "Qualitative and quantitative detection of pesticides with terahertz time-domain spectroscopy," *IEEE Trans. Microw. Theory Techn.*, vol. 58, no. 7, pp. 2064–2070, Jul. 2010.
- [6] H. Liu *et al.*, "Dimensionality reduction for identification of hepatic tumor samples based on terahertz time-domain spectroscopy," *IEEE Trans. Terahertz Sci. Technol.*, vol. 8, no. 3, pp. 271–277, May 2018.
- [7] D. Brigada and X. Zhang, "Chemical identification with information-weighted terahertz spectrometry," *IEEE Trans. THz Sci. Technol.*, vol. 2, no. 1, pp. 107–112, Jan. 2012.
- [8] X. Wei, S. Zhu, S. Zhou, W. Zheng, and S. Li, "Identification of soybean origin by terahertz spectroscopy and chemometrics," *IEEE Access*, vol. 8, pp. 184988–184996, 2020.
- [9] M. S. Islam *et al.*, "Experimental study on glass and polymers: Determining the optimal material for potential use in terahertz technology," *IEEE Access*, vol. 8, pp. 97204–97214, 2020.
- [10] F. Lian *et al.*, "Identification of transgenic ingredients in maize using terahertz spectra," *IEEE Trans. THz Sci. Technol.*, vol. 7, no. 4, pp. 378–384, Jul. 2017.
- [11] C. Li, B. Li, and D. Ye, "Analysis and identification of rice adulteration using terahertz spectroscopy and pattern recognition algorithms," *IEEE Access*, vol. 8, pp. 26839–26850, 2020.

- [12] A. D. van Rheenen and M. W. Haakestad, "Robust identification of concealed dangerous substances by spectral correlation of terahertz transmission images," *IEEE Trans. THz Sci. Technol.*, vol. 5, no. 3, pp. 438–444, May 2015.
- [13] H. Morimoto and S. Kidera, "Super-resolution multilayer structure analysis via depth adaptive compressed sensing for terahertz subsurface imaging," *IEEE Geosci. Remote Sens. Lett.*, to be published.
- [14] L. Wang, Z. Cao, Z. Cui, C. Cao, and Y. Pi, "Negative latency recognition method for fine-grained gestures based on terahertz radar," *IEEE Trans. Geosci. Remote Sens.*, vol. 58, no. 11, pp. 7955–7968, Nov. 2020.
- [15] R. Xie and J. Cao, "Accelerometer-based hand gesture recognition by neural network and similarity matching," *IEEE Sens. J.*, vol. 16, no. 11, pp. 4537–4545, Jun. 2016.
- [16] K. Li, X. Chen, R. Zhang, and E. Pickwell-MacPherson, "Classification for glucose and lactose terahertz spectrums based on SVM and DNN methods," *IEEE Trans. THz Sci. Technol.*, vol. 10, no. 6, pp. 617–623, Nov. 2020.
- [17] M. Moller, "A scaled conjugate gradient algorithm for fast supervised learning," *Neural Netw.*, vol. 6, no. 4, pp. 525–533, 1993.
- [18] Z. Li, N. Wang, Y. Li, X. Sun, M. Huo, and H. Zhang, "Collective efficacy of support vector regression with smoothness priority in marine sensor data prediction," *IEEE Access*, vol. 7, pp. 10308–10317, 2019.
- [19] D. Rodriguez, M. A. Saed, and C. Li, "A WPT/NFC-based sensing approach for beverage freshness detection using supervised machine learning," *IEEE Sens. J.*, vol. 21, no. 1, pp. 733–742, Jan. 2021.
- [20] B. Ibragimov and L. Xing, "Segmentation of organs-at-risks in head and neck CT images using convolutional neural networks," *Med. Phys.* vol. 44, no. 2, pp. 547–557, Dec. 2016.



Takamaru Matsui received the B.E. degree in communication engineering and informatics from the University of Electro-Communications, Tokyo, Japan, in 2018, and received the M. E degree with the Graduate School of Informatics and Engineering, the University of Electro-Communications, Tokyo, Japan, in 2020. He joined the Ricoh Co.,Ltd., 2020.



Shouhei Kidera received the B.E. degree in electrical and electronic engineering from the Kyoto University in 2003 and the M.I. and Ph.D. degrees in informatics from Kyoto University, Kyoto, Japan, in 2005 and 2007, respectively. He has been with Graduate School of Informatics and Engineering, the University of Electro-Communications, Tokyo, Japan, since 2009, and is currently an Associate Professor. His current research interest is in advanced radar signal processing or electromagnetic inverse scattering issue for ultra wideband (UWB) three-dimensional sensor or bio-medical applications. He has been associated with the Cross-Disciplinary Electromagnetics Laboratory in the University of Wisconsin Madison as the Visiting Researcher in 2016. He has been a Principal Investigator of the PRESTO Program of Japan Science and Technology Agency (JST) from 2017 to 2021. He was a recipient of the 2012 Ando Incentive Prize for the Study of Electronics, 2013 Young Scientist's Prize by the Japanese Minister of Education, Culture, Sports, Science and Technology (MEXT), and 2014 Funai Achievement Award. He is a Senior Member of the Institute of Electronics, Information, and Communication Engineers of Japan (IEICE), and a Member of the Institute of Electrical Engineering of Japan (IEEJ), and the Japan Society of Applied Physics (JSAP).



Kanto Kito received the B.E. degree in communication engineering and informatics from the University of Electro-Communications, Tokyo, Japan, in 2021.